



The viscosity of Earth's lower mantle inferred from sinking speed of subducted lithosphere

Hana Čížková^{a,*}, Arie P. van den Berg^b, Wim Spakman^b, Ctirad Matyska^a

^a Faculty of Mathematics and Physics, Charles University Prague, V Holešovičkách 2, 18000 Praha 8, Czech Republic

^b Institute of Earth Sciences, Utrecht University, Budapestlaan 4, 3584 CD Utrecht, The Netherlands

ARTICLE INFO

Article history:

Received 20 October 2011

Received in revised form 27 January 2012

Accepted 10 February 2012

Available online 20 February 2012

Keywords:

Lower mantle viscosity

Slab sinking velocity

ABSTRACT

The viscosity of the mantle is indispensable for predicting Earth's mechanical behavior at scales ranging from deep mantle material flow to local stress accumulation in earthquakes zones. But, mantle viscosity is not well determined. For the lower mantle, particularly, only few constraints result from elaborate high-pressure experiments (Karato, 2008) and a variety of viscosity depth profiles result from joint inversion of the geoid and postglacial rebound data (Forte and Mitrović, 1996; Kaufmann and Lambeck, 2000; Mitrović and Forte, 2004). Here, we use inferred lower-mantle sinking speed of lithosphere subduction remnants as a unique internal constraint on modeling the viscosity profile. This entails a series of elaborate dynamic subduction calculations spanning a range of viscosity profiles from which we select profiles that predict the inferred sinking speed of 12 ± 3 mm/yr (van der Meer et al., 2010). Our modeling shows that sinking speed is very sensitive to lower mantle viscosity. Good predictions of sinking speed are obtained for nearly constant lower mantle viscosity of about $3\text{--}4 \times 10^{22}$ Pa s. Viscosity profiles incorporating a viscosity maximum in the deep lower mantle, as proposed in numerous studies, only lead to a good prediction in combination with a weak postperovskite layer at the bottom of the lower mantle, and only for a depth average viscosity of 5×10^{22} Pa s.

© 2012 Elsevier B.V. All rights reserved.

1. Introduction

In the Earth's mantle, solid-state creep facilitates buoyancy driven material flow on the scale of centimeters per year across the entire mantle. Viscosity characterizes the internal friction of the flow and is one of the key quantities determining the mechanical behavior of the mantle. The latter governs global plate tectonics and is also fundamental for quantifying the coupling between mantle processes and surface deformation. This includes deep processes leading to earthquakes and volcanoes, or the solid Earth contribution to sea level change, today, or in the future.

Viscosity can be estimated from a combination of theory and experiment based on the deformation mechanism acting at the atomic scale (Karato, 2008). However, present uncertainty about critical material properties, e.g. activation volumes and -energies under the high pressure and temperature conditions of the mantle, about the precise composition of the mantle, and about extrapolation of experimental results to mantle conditions, render viscosity estimates of unknown accuracy.

Alternatively, many studies of the past decades estimate the mantle viscosity profile from a joint geophysical inversion of

mantle structure, the geoid, and/or vertical surface motion data associated with the solid earth response to ice sheet (un)loading and sea level change, heat flow, or dynamic surface topography (e.g. Ricard and Vigny, 1989; Pari and Peltier, 1995; Forte and Mitrović, 1996; Panasyuk and Hager, 2000; Steinberger and Calderwood, 2006). These studies resulted in quite a range of viscosity-depth profiles possibly reflecting the weak sensitivity of the input data and models for (depth)variations in viscosity (see Fig. 1c).

Here, we propose a novel avenue of determining deep mantle viscosity made possible by recent work on correlating deep mantle structure with the plate tectonic evolution of the past 300 Myr (van der Meer et al., 2010). A spin-off of that study is the first empirical estimate of the average sinking speed (12 ± 3 mm/yr) of remnants of subducted lithosphere in the lower mantle during the past 300 Myr. Sinking speed depends on mantle viscosity. We perform numerical experiments designed to infer the lower mantle viscosity by modeling the descent of sinking remnants of negatively buoyant lithosphere material. The simplest of such experiments would be to determine the terminal velocity of a Stokes sinking sphere (Morgan, 1965), which e.g. would yield 1 cm/yr for a sphere with radius of 200 km and 0.5% excess density sinking in a fluid with viscosity of about 6×10^{22} Pa s. Such a back of envelope calculation can, however, only give a rough order of magnitude estimate for iso-viscous fluids and cannot account for depth-dependent viscosity, the more complex geometry of the sinking slab remnants, the fact that the

* Corresponding author. Tel.: +420 221912544.

E-mail address: Hana.Cizkova@mff.cuni.cz (H. Čížková).

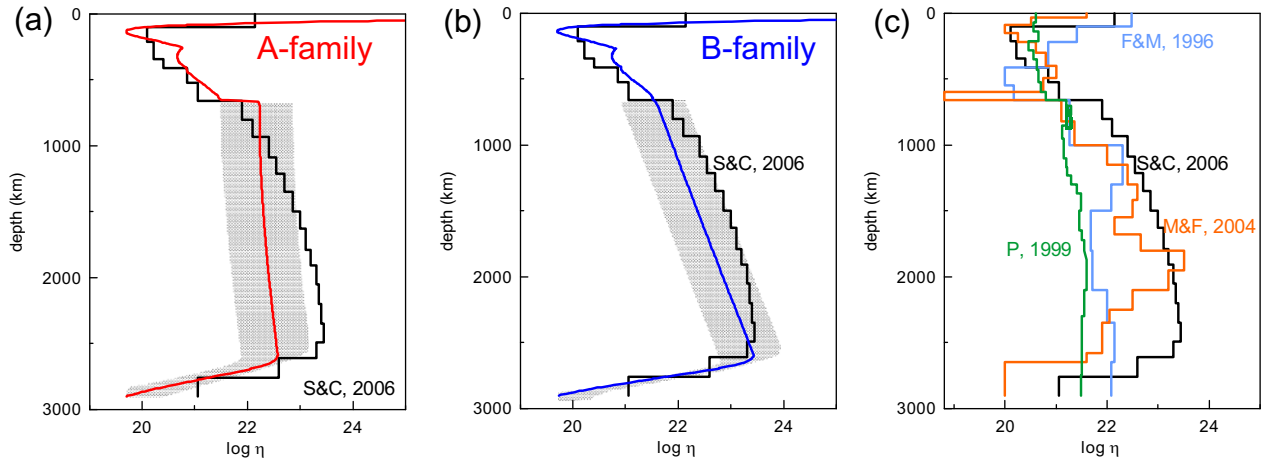


Fig. 1. Viscosity models used in this study. (a) Family A models with viscosity almost constant with depth. Gray area depicts the range of the lower mantle viscosity stratifications controlled by the viscosity prefactor A_{diff} (Supplementary Table 2). The horizontally averaged viscosity in the initial state is shown. For reference, one of the viscosity profiles of Steinberger and Calderwood (2006) is also shown (black line). (b) Family B models with a maximum at about 2500 km depth. (c) Viscosity profiles based on the joint inversion of the geoid and postglacial rebound data. F&M 1996 – Forte and Mitrovia (1996), P 1999 – Peltier (1999), M&F 2004 – Mitrovia and Forte (2004), S&C 2006 – Steinberger and Calderwood (2006).

terminal velocity may be quite sensitive to the density anomaly while the density anomaly itself is a complex function of the Earth's material parameters (viscosity, thermal expansivity) and the history of subduction (e.g. the delay and associated warming at the 660 km interface).

Our modeling experiments focus on converting sinking speed to mantle viscosity for which we perform detailed two-dimensional (2-D) subduction modeling experiments mimicking subduction evolution from top to bottom of the mantle. We aim for (1) establishing the sensitivity of the sinking speed of slab remnants for variations in lower mantle viscosity, and for (2) determining viscosity profiles that are consistent with the inferred sinking rate.

2. Methods

In our numerical model setup we use an extended Boussinesq model of the mantle evolution to track the subducting slabs. A detailed description of the governing equations and numerical method is given in Čížková et al. (2007). The 2-D model domain is a rectangular box with the depth of the mantle (2900 km) and width of 10,000 km. We have a 5000 km long subducting plate stretching between the mid-ocean ridge in the upper-left corner of the model domain and the trench (Běhounková and Čížková, 2008). The initial temperature distribution within the plate is given by the half-space model. The plate is 100 Myr old at the trench. To the right from the trench there is an overriding plate with a constant thickness corresponding to the thickness of a subducting plate at the trench. Below the plates an initial adiabatic temperature profile is prescribed with a potential temperature of 1573 K. Above the core-mantle boundary a 300 km wide thermal boundary layer is assumed with temperature rising from the foot of the adiabat to the CMB temperature of 4000 K. On the top of the subducting plate we prescribe a 15 km thick crust-like layer. Its constant low viscosity (10^{20} Pa s) enables the decoupling of the subducting and overriding plates. Viscosity of crustal material is computed using particle tracers that are advected by the mantle convective flow (Běhounková and Čížková, 2008). In this model set up (mainly facilitated by the weak crustal layer) one-sided subduction is generated in a natural way, without prescribing either a fixed weak zone (e.g. King and Hager, 1994) or a lithospheric fault (Zhong and Gurnis, 1995; van Hunen et al., 2000; Čížková et al., 2002). This way crustal material is tracked down to the depth of 200 km,

where it is replaced by the mantle material for numerical convenience. There is no additional buoyancy contribution associated with this crustal layer. A short initial run is executed with a prescribed velocity of 5 cm/yr on the top of the subducting plate in order to obtain a developed slab tip reaching the depth of about 200 km. This developed slab configuration is then used as an initial condition for the actual model runs. Free-slip conditions are prescribed on all boundaries.

The analysis of van der Meer et al. (2010) mostly refers to the sinking velocities of the detached slabs, therefore we concentrate on them in our models as well. In order to simulate a break-off of the subducting slab we suppress the decoupling between the subducting and overriding plates. To this end we assume that the weak crust initially extends only 2000 km to the left from the trench. When the plate segment covered with this weak crust is subducted, the friction on the contact of subducting and overriding plates enforces the locking of the subducting plate and the break-off follows.

3. Model parameters

Our rheological description combines diffusion creep, dislocation creep and a power-law stress limiter (see below) in a composite model (e.g. van Hunen et al., 2002). Assuming a unique stress, the effective viscosity is given by the following relation (van den Berg et al., 1993):

$$\eta_{eff} = \left(\frac{1}{\eta_{diff}} + \frac{1}{\eta_{disl}} + \frac{1}{\eta_y} \right)^{-1} \quad (1)$$

The viscosities of the diffusion and dislocation creep η_{diff} and η_{disl} are defined through Arrhenius laws:

$$\eta_{diff} = \frac{1}{A_{diff}} \exp \left(\frac{E_{diff} + pV_{diff}}{RT} \right) \quad (2)$$

$$\eta_{disl} = \frac{1}{A_{disl}^n} e^{(1-n)/n} \exp \left(\frac{E_{disl} + pV_{disl}}{nRT} \right) \quad (3)$$

Symbols and corresponding values are listed in Table 1. A stress limiter viscosity is defined as:

$$\eta_y = \tau_y e_y^{-1/n_y} e^{1/n_y - 1} \quad (4)$$

Table 1
Model parameters.

Symbol	Meaning	Value	Units
<i>Upper mantle rheology</i>			
A_{diff}	Pre-exponential parameter of diffusion creep	1×10^{-9}	$\text{Pa}^{-1} \text{s}^{-1}$
A_{dist}	Pre-exponential parameter of dislocation creep	3.1×10^{-17}	$\text{Pa}^{-n} \text{s}^{-1}$
E_{diff}	Activation energy of diffusion creep	3.35×10^5	J mol^{-1}
E_{dist}	Activation energy of dislocation creep	4.8×10^5	J mol^{-1}
V_{diff}	Activation volume of diffusion creep	4.8×10^{-6}	$\text{m}^3 \text{mol}^{-1}$
V_{dist}	Activation volume of dislocation creep	11×10^{-6}	$\text{m}^3 \text{mol}^{-1}$
n	Power-law exponent	3.5	–
η_{crust}	Viscosity of crust	10^{20}	Pa s
τ_y	Yield stress	5×10^8	Pa
e_y	Reference strainrate	1×10^{-15}	s^{-1}
n_y	Stress limiter exponent	10	–
P	Hydrostatic pressure	–	–
R	Gas constant	8.314	$\text{J K}^{-1} \text{mol}^{-1}$
T	Temperature	–	–
E	Second invariant of the strainrate	–	s^{-1}
<i>Lower mantle rheology Family A</i>			
A_{diff}	Pre-exponential parameter of diffusion creep	$5 \times 10^{-17} - 1 \times 10^{-15}$	$\text{Pa}^{-1} \text{s}^{-1}$
E_{diff}	Activation energy of diffusion creep	2×10^5	J mol^{-1}
V_{diff}	Activation volume of diffusion creep	1.1×10^{-6}	$\text{m}^3 \text{mol}^{-1}$
<i>Lower mantle rheology Family B</i>			
A_{diff}	Pre-exponential parameter of diffusion creep	$1.8 \times 10^{-15} - 2.3 \times 10^{-14}$	$\text{Pa}^{-1} \text{s}^{-1}$
E_{diff}	Activation energy of diffusion creep	2×10^5	J mol^{-1}
V_{diff}	Activation volume of diffusion creep	2.2×10^{-6}	$\text{m}^3 \text{mol}^{-1}$
η_{PPV}	Postperovskite viscosity	10^{21}	Pa s
<i>Other model parameters</i>			
κ	Diffusivity	10^{-6}	$\text{m}^2 \text{s}^{-1}$
G	Gravitational acceleration	9.8	m s^{-2}
ρ_0	Reference density	3416	kg m^{-3}
c_p	Specific heat	1250	$\text{J kg}^{-1} \text{K}^{-1}$
α_0	Surface thermal expansivity	3×10^{-5}	K^{-1}
$\Delta\alpha$	Expansivity contrast	0.3	–
γ_{410}	Clapeyron slope 410 km phase transition	3×10^6	Pa K^{-1}
γ_{660}	Clapeyron slope 660 km phase transition	-2.5×10^6	Pa K^{-1}
γ_{PPV}	Clapeyron slope PPV phase transition	9×10^6	Pa K^{-1}
T_{int}	Temperature intercept PPV phase transition	3000	K
$\delta\rho_{410}$	Density contrast 410 km phase transition	273	kg m^{-3}
$\delta\rho_{660}$	Density contrast 660 km phase transition	341	kg m^{-3}
$\delta\rho_{PPV}$	Density contrast PPV phase transition	34	kg m^{-3}

with the stress limiter index $n_y = 10$. This stress limiting mechanism effectively replaces more sophisticated mechanisms as the low-temperature plasticity (Peierls creep). The yield stress of the subducting slabs is assumed to be 0.5 GPa, which corresponds to the yield strength of olivine at about 900 °C (Billen, 2010). The rheological description in our models varies among different phases. Thus the upper mantle, lower mantle and postperovskite (if present) have different activation parameters. The upper mantle and the transition zone deform via diffusion creep, dislocation creep and the stress limiter with the activation parameters based on Hirth and Kohlstedt (2003). They produce a viscosity contrast of about 4–5 orders of magnitude between the slab and ambient mantle in the transition zone.

Dislocation creep is usually assumed to play only a minor role in the lower mantle (Karato et al., 1995), therefore we assume here that the lower mantle deforms exclusively via diffusion creep (van den Berg and Yuen, 1996). We define two distinct families (A and B) of viscosity profiles based on two sets of lower mantle diffusion creep activation parameters (Table 1): one yielding lower mantle viscosity almost constant with depth as proposed, e.g. by Peltier (1999) (A-family, Fig. 1a) and the other with a viscosity maximum at a depth of about 2500 km (B-family, Fig. 1b) as suggested by several studies (Ricard and Wuming, 1991; Mitrovica and Forte, 2004; Steinberger and Calderwood, 2006). Fig. 1c illustrates the variety of the viscosity profiles that recently appeared

as the results of the geoid and/or postglacial data inversions. The spread between these profiles demonstrates the current uncertainty particularly in the viscosity of the lower mantle. Moreover, as recently pointed out by Paulson et al. (2007), the resolving power for mantle viscosity in inversions of the postglacial rebound data is limited to a two layer viscosity profile giving one value for the upper mantle and one value for the lower mantle. From each set of parameters we generate a range of viscosity profiles spanning the shaded area in Fig. 1, which is controlled by the pre-factor of the diffusion-creep viscosity, including a viscosity jump at 660 km depth. The activation energies applied in our models imply a viscosity contrast of 2–3 orders of magnitude between the slab and the ambient mantle in the upper part of the lower mantle (~1000 km depth). The relatively weak slabs are thus easy to deform and significant buckling is observed. The temperature contrast of the slab is decreasing due to thermal assimilation as the detached slab descends through the lower mantle and as a result the temperature difference between the core of the slab and the ambient mantle is less than 600 K just below the 660 km boundary and about 500 K at 2000 km depth. The viscosity contrast is then about 2 orders of magnitude at 2500 km depth.

For some models of the B-family, we also investigate a possible flow accelerating effect of rheologically weak postperovskite present near the bottom of the mantle. Postperovskite may be characterized by a significantly lower viscosity compared to the

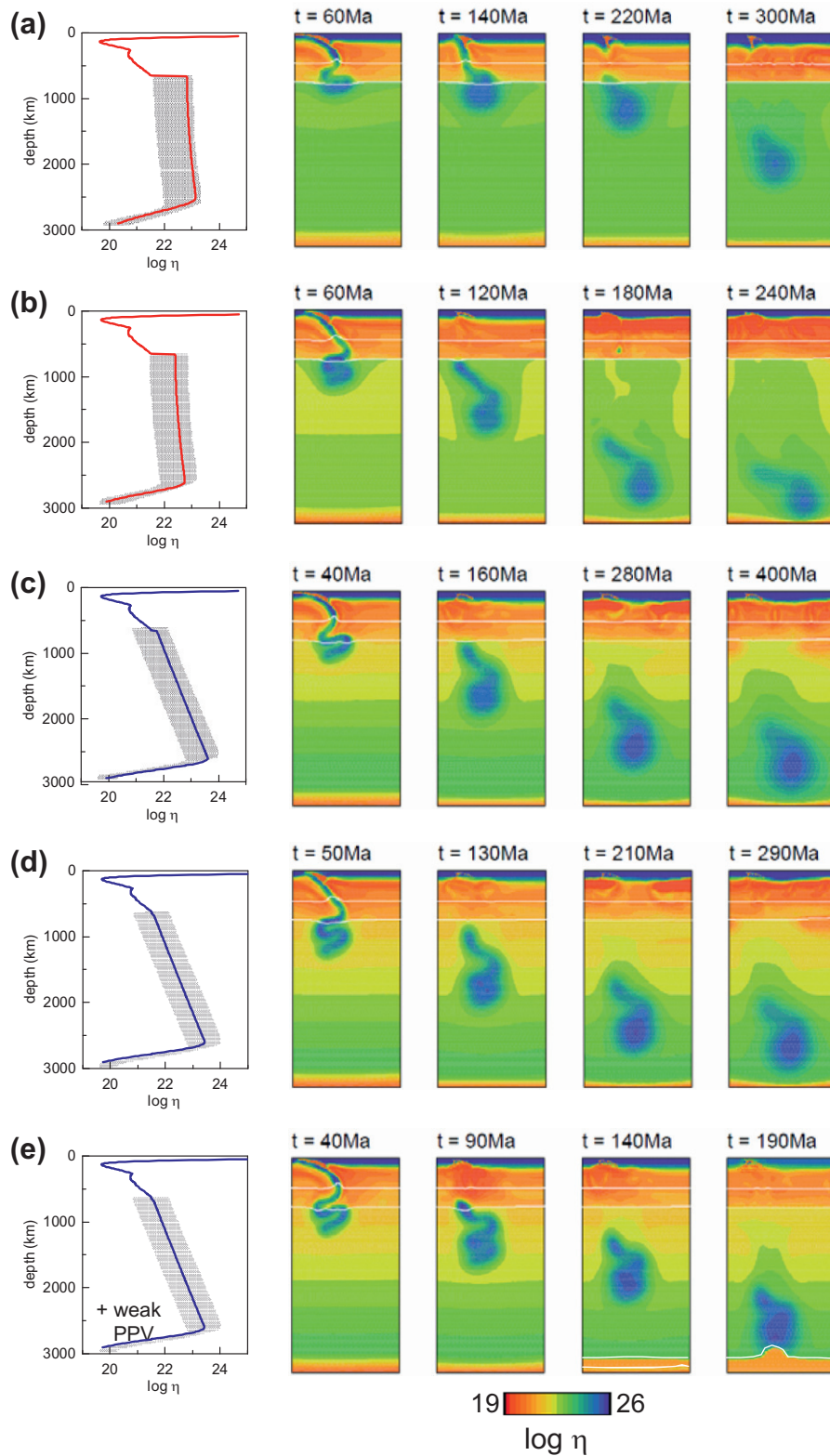


Fig. 2. Time evolution of the slabs in five selected models. The first panel in each row shows the depth viscosity profile of a given model, next four panels give the time evolution of the logarithm of effective viscosity. Only a part of the model domain 1500 km wide and 2900 km deep centered around the slab is shown. White lines indicate the positions of the major mantle phase transitions near the depths of 410 and 660 km and the postperovskite phase transition. (a) Model of A family with a volume average lower mantle viscosity $\eta_{aver} = 8.10^{22}$ Pa s, (b) model of A family with $\eta_{aver} = 3.1 \times 10^{22}$ Pa s, (c) model of B family with $\eta_{aver} = 7.6 \times 10^{22}$ Pa s, (d) model of B family with $\eta_{aver} = 5 \times 10^{22}$ Pa s, (e) the same as (d) but with a weak postperovskite. Volume average viscosity is calculated with spherical geometry.

background perovskite mantle (Ammann et al., 2010; Čížková et al., 2010; Nakagawa and Tackley, 2011). Here, we assign a constant viscosity of 10^{21} Pa s to postperovskite phase.

Thermal expansivity of representative mantle material is decreasing with depth from a surface value of approximately 3×10^{-5} to $1 \times 10^{-5} \text{ K}^{-1}$ at the CMB (Chopelas and Boehler, 1992;

Katsura et al., 2009) following the formula (Hansen and Yuen, 1994; Steinbach and Yuen, 1994):

$$\alpha = \alpha_0 \frac{\Delta\alpha}{[(\Delta\alpha^{1/3} - 1)(1 - z) + 1]^3} \quad (5)$$

Here, α_0 is the surface value, $\Delta\alpha$ the contrast over the mantle and z is the dimensionless depth (see Table 1).

Temperature dependence of thermal expansivity is smaller than its pressure dependence and it also decreases with increasing pressure. Since the primary focus of this paper is the estimate of the rheological effects on the sinking speed of subducting slabs, we apply a purely depth/pressure dependent parameterization of α and leave a more elaborate investigation of its effects to future work.

4. Results

The dynamically self-consistent subduction histories comprise upper mantle subduction, interactions with major phase changes, buckling and thickening of slab material, temporal stagnation at the top of the lower mantle, and eventually sinking through the deep mantle. Typical modeling results are presented in Fig. 2 for several rheological profiles. Fig. 2a shows a model from the A-family characterized by a viscosity increase of a factor of 18 at 660 km. Due to the combined effect of the major mantle phase transitions at the depths of 410 and 660 km the slab buckles in the top of the lower mantle forming a thick, amorphous structure. This transition from more plate-like upper mantle slabs to broad amorphous structures in the lower mantle is also observed by mantle tomography (van der Hilst, 1995; Bijwaard et al., 1998). We should note here that the presence of both exothermic and endothermic phase transitions is crucial in order to form the thick buckled structure in agreement with the tomographic indications. Particularly, the absence of the 410 km phase transition, normally enhancing the slab descent results in reduced or no buckling (Běhounková and Čížková, 2008). Relatively thin slab then would then penetrate more easily to the lower mantle. The slab breaks off at 170 Myr but the detached part remains temporally stagnant below the 660 km phase boundary (Fukao et al., 2001) and then it descends slowly through the lower mantle. After 300 Myr the detached part of the slab arrives at the mid-lower mantle. Lowering the viscosity contrast associated with the 660 km phase transition from a factor of 18–7, reduces the time delay of the detached slab segment at the

660 km boundary to less than 10 Myr, while the descent through the lower mantle is much faster yielding arrival at the CMB within about 240 Myr (Fig. 2b). The speed up is due to the reduced resistance of the weaker lower mantle. A model representing viscosity profiles from the B-family is shown in Fig. 2c. This viscosity model has only a very mild step change of viscosity (factor 1.5) associated with the 660 km boundary, but the effects of the major mantle phase transitions followed by a gradual viscosity increase just below 660 km again cause the slab to buckle prior to the detachment. After break-off the slab starts a slow descent through the lower mantle owing to the relatively high viscosity and reaches the bottom of the lower mantle within 400 Myr. Lowering the lower mantle viscosity by only a factor of 0.65 (Fig. 2d) results in a considerably faster slab descent (cf. the last panels of Fig. 2c and d). When a postperovskite mineral phase is added, weak patches (about 150 km thick) appear near the bottom of the model below the downgoing slab material (Fig. 2e) and the detached slab arrives at the CMB even faster. One should note here that the speeding-up effect of the weak postperovskite is observed before the slab actually arrives at the D'' . That is due to the fact, that as the cold slab is descending, relatively cool material is entering the warm bottom boundary layer thereby crossing the postperovskite phase boundary. This already occurs when the slab itself is still several hundreds of kilometres above the bottom boundary.

To determine the average sinking speed and its temporal and spatial variability we use tracers initially placed into the part of the slab that is going to detach (see Section 2). This group of tracers is then tracked during its descent through the mantle. We track the behavior of the center of the tracer group minimizing effects of buckling, rotations, or stretching of the detached segment. Fig. 3a shows age–depth paths of the tracer center for different viscosity profiles of A- (red) and B-family (blue) (cf. Fig. 1a and b). The gray area depicts the age–depth envelope of data points as interpreted by van der Meer et al. (2010) and represents our ‘target area’ for tracer centers consistent with the sinking rate of 12 ± 3 mm/yr. Numbers labeling each curve give the model average of lower mantle viscosity. Curves resulting from profile A (red curves) yield a very slow descent for the higher viscosities. In the most viscous lower mantle ($\eta_{aver} = 8 \times 10^{22}$ Pa s), the detached slab only reach a depth of 1000 km within 250 Myr, while in the weakest lower mantle ($\eta_{aver} = 8.4 \times 10^{21}$ Pa s) the detached slab arrives at the bottom within less than 100 Myr. Temporal slab stagnation is reflected in the plateau present in the models with $\eta_{aver} > 3.1 \times$

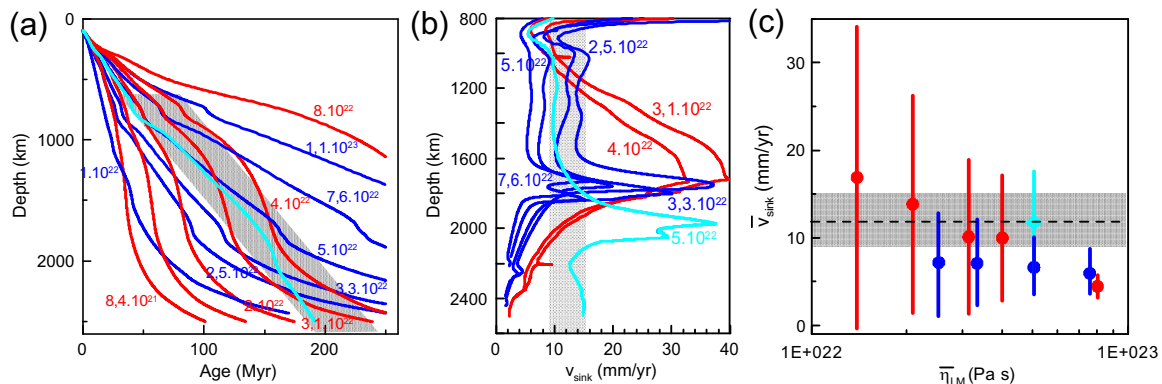


Fig. 3. Sinking velocity. (a) Depth versus age curves for models of A-family (red curves) and B-family (blue curves). Red and dark blue lines are for models without postperovskite, light blue depicts corresponding model with a low viscosity postperovskite. The gray area represents the sinking velocities inferred by van der Meer et al. (2010). The curves are plotted for the center of the detached slab segment. Numbers associated with the curves give the volume average lower mantle viscosity of the models. (b) Sinking velocities for the same models as in (a) as a function of depth in the lower mantle. They are only shown for the time window up to 250 Myr since the onset of subduction. Gray area represents the bounds given by van der Meer et al. (2010). (c) Average sinking velocities plotted as a function of the volume average lower mantle viscosity. The average is calculated over the time window between the break-off and 250 Myr since the onset of subduction. Red dots are for the models of A-family without postperovskite, blue dots are for models of B-family without postperovskite and light blue diamond for B-type model with a weak postperovskite. Volume average viscosity is calculated with spherical geometry. (For interpretation of the references to color in this figure legend, the reader is referred to the web version of this article.)

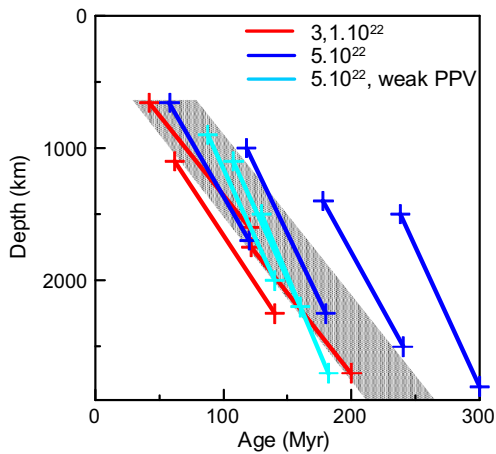


Fig. 4. Age–depth curves. Age–depth curves for several stages of slab sinking in best fitting models. Each curve represents one snapshot, the age of its upper point is measured since the break-off moment, the lower point since the onset of subduction.

10^{22} Pa s. Among the red curves in Fig. 3a two models fit the gray target region and have a lower mantle viscosity of $3.1\text{--}4 \times 10^{22}$ Pa s. Viscosity profiles belonging to the B family give similar results up to depths of 1000 km. In the deeper mantle, however, the slab slows down significantly owing to the gradually increasing viscosity. As a result the age–depth curves do not fit the target area (dark blue curves). Including a weak postperovskite layer enhances the flow in the lowermost mantle and increases the sinking velocities (light blue line). Thus B-model with an average lower mantle viscosity of about 5×10^{22} Pa s and a weak postperovskite is also in agreement with the inferred sinking speed.

The depth variability of the sinking rate is further demonstrated in Fig. 3b. The models of the A family (red curves) start at a low sinking value while the detached slab segments are stagnant at the 660 km phase boundary. Next, the sinking speed increases and reaches its maximum around 1600 km after which it gradually slows down as the slab is approaching the bottom of the mantle. The sinking velocities of models B (blue lines) are usually almost uniform in the upper half of the lower mantle and then after reaching local maxima around 1600 km drop significantly as the slab approaches the viscosity maximum at 2500 km depth if no weak material is assumed in the D'' (dark blue lines). Model including a weak postperovskite (light blue line) on the other hand experiences an increased sinking velocity below 2000 km depth.

Our results are differently condensed in Fig. 3c focusing on average sinking speed which is plotted against average lower mantle viscosity. The sinking speed is averaged over a time window starting at the break-off and ending at 250 Myr after the onset of subduction. The models of group A (red dots) show a systematic decrease of an average sinking rate with increasing lower mantle viscosity. At the same time the spread in sinking speeds decreases thus reflecting the fact that in the weaker lower mantle sinking speed can be more variable with depth while it is more uniform in a stiffer mantle. In all models of the B family without postperovskite (dark blue dots) the sinking speed is too small. Including a weak postperovskite, however, shifts it toward the target value (Fig. 3c, light blue diamond).

Fig. 4 follows closely the representation of van der Meer et al. (2010), who plotted the depths of bottom and top of tomographically imaged slab remnants versus the age of subduction start and of the slab detachment, respectively. Similar information can be inferred from snapshots of our modeled subduction histories and is presented in Fig. 4, showing different snapshots for three models: the best fitting A-model (red), best fitting B-model without post-

perovskite (dark blue)¹ and the best fitting B-model including weak postperovskite (light blue). Fig. 4 shows that the preferred A-model fits the gray target area well. The B-models only yield a successful solution if weak postperovskite is present in the lowermost mantle including the slab.

5. Discussion and conclusions

Our best-fitting viscosity profiles are associated with subduction models that show accumulation or thickening of the slab, but minor temporal stagnation associated with the phase change at 660 km and a mild increase of viscosity in the top of the lower mantle by a factor of three. The sinking speed constrains almost uniform viscosity models of the lower mantle to a viscosity value of $3\text{--}4 \times 10^{22}$ Pa s. Higher amplitudes of the lower mantle viscosity (and an associated step-wise increase at the 660 km phase boundary) are responsible for the detached slab being stagnant for 10 s of millions of years at the top of the lower mantle (Jarvis and Lowman, 2007). This yields a corresponding delay in age–depth curves and leads to average deviating from the inferences of van der Meer et al. (2010). A weaker lower mantle, on the other hand, produces slabs that are too fast and reach the base of the mantle in much less than 200 Myr.

We found that the gradual viscosity increase characterizing the B-family of profiles reduces the sinking velocities in the deep lower mantle to values too much different from the target value. The viscosity maximum suggested by numerous studies (e.g. Ricard and Wuming, 1991; Mitrovica and Forte, 2004; Steinberger and Calderwood, 2006; Matyska et al., 2011) results in slowing down of slab remnants below a depth of 1600 km. In order to obtain the average lower mantle sinking rate of the order 1 cm/yr we then need viscosity reduction in the D'' . The low viscosity anomalies at the bottom boundary layer are in agreement with inferences of Čadek and Fleitout (2006) and could be explained by the presence of weak postperovskite (Ammann et al., 2010) or by the steep temperature gradient in the D'' layer (Hernlund et al., 2005) or high thermal conductivity (Matyska et al., 2011), or a combination of these. Significant viscosity reduction within the D'' has recently indeed been reported by Nakada and Karato (submitted for publication) based on the Chandler wobble analysis. Our preferred B-family model with weak postperovskite is characterized by a volume-average lower mantle viscosity of about 5×10^{22} Pa s.

The analysis of Van der Meer et al. (2010) derives the sinking speed of the detached slabs freely falling through the (lower) mantle. Therefore, our numerical experiments have been carried out in the models where slab remnants sink through the lower mantle disconnected from the upper mantle subduction. If a continuous subduction is assumed the slab sinking velocities may be substantially higher (Steinberger and Torsvik, 2010). In case of our preferred model of A family sinking rate in the lower mantle is higher by about a factor 2 if subduction continues at the same place until the slab reaches the CMB. Van der Meer et al. (2010) could, however, not infer such modes of long standing continuous subduction reaching from the surface to core-mantle boundary, not from the geological record of the past ~ 500 My and also not from the tomographic model used.

Our results are inevitably influenced by a 2D Cartesian simplification. Nevertheless, we believe that the presented models provide a reasonable estimate of the realistic sinking rates. These seem to be in agreement with the rates obtained in 3D convection calculations with the density anomalies based on the paleoslab recon-

¹ For interpretation to color in the text, the reader is referred to the web version of this article.

structions (Steinberger and Torsvik, 2011) if detached slabs are considered (Steinberger, personal communication). The effect of the realistic 3D geometry should however be subject to further research.

Our results clearly demonstrate that the sinking speed of slab remnants is very sensitive to the viscosity structure of the lower mantle and thus provides a strong constraint on lower mantle viscosity. More accurate determination of sinking speeds, e.g. obtained from a more detailed analysis along lines of van der Meer et al. (2010), or modeling differently constrained slab–mantle interaction (Spakman and Hall, 2010), is a promising road to improve estimates of the viscosity of the mantle, and in combination with mineral physics research may help in disclosing underlying material properties.

Acknowledgements

We thank Bernhard Steinberger and Shijie Zhong for constructive reviews that helped to improve the manuscript. This research has been supported by the Czech Science Foundation Grant P210/11/1366, by the Research Project MSM0021620860 of the Czech Ministry of Education and the Netherlands Research School for Integrated Solid Earth Science (ISES). This paper contributes to the ESF EUROCORES programme TOPO-EUROPE.

Appendix A. Supplementary data

Supplementary data associated with this article can be found, in the online version, at <http://dx.doi.org/10.1016/j.pepi.2012.02.010>.

References

- Ammann, M.W., Brodholt, J.P., Wookey, J., Dobson, D.P., 2010. First-principles constraints on diffusion in lower-mantle minerals and a weak D'' layer. *Nature* 465, 462–465.
- Bijwaard, H., Spakman, W., Engdahl, E.R., 1998. Closing the gap between regional and global travel time tomography. *J. Geophys. Res.* 103, 30055–30075.
- Billen, M., 2010. Slab dynamics in the transition zone. *Phys. Earth Planet. Inter.* 183, 296–308.
- Běhouňková, M., Čížková, H., 2008. Long-wavelength character of subducted slabs in the lower mantle. *Earth Planet. Sci. Lett.* 275, 43–53.
- Chopelas, A., Boehler, R., 1992. Thermal expansivity in the lower mantle. *Geophys. Res. Lett.* 19, 1983–1986.
- Čadek, O., Fleitout, L., 2006. Effect of lateral viscosity variations in the core–mantle boundary region on predictions of the long-wavelength geoid. *Stud. Geophys. Geod.* 50, 217–232.
- Čížková, H., van Hunen, J., van den Berg, A.P., Vlaar, N.J., 2002. The influence of rheological weakening and yield stress on the interaction of slabs with the 670-km discontinuity. *Earth Planet. Sci. Lett.* 199, 447–457.
- Čížková, H., van Hunen, J., van den Berg, A.P., 2007. Stress distribution within subducting slabs and their deformation in the transition zone. *Phys. Earth Planet. Inter.* 161, 202–214.
- Čížková, H., Čadek, O., Matyska, C., Yuen, D.A., 2010. Implications of postperovskite transport properties for core–mantle dynamics. *Phys. Earth Planet. Inter.* 180, 235–243.
- Forte, A., Mitrovica, J., 1996. New inferences of mantle viscosity from joint inversion of long-wavelength convection and post-glacial rebound data. *Geophys. Res. Lett.* 23, 1147–1150.
- Fukao, Y., Widiyantoro, S., Obayashi, M., 2001. Stagnant slabs in the upper and lower mantle transition region. *Rev. Geophys.* 39, 291–323.
- Hansen, U., Yuen, D.A., 1994. Effects of depth-dependent thermal expansivity on the interaction of thermal–chemical plumes with a compositional boundary. *Phys. Earth Planet. Inter.* 86, 205–221.
- Hirth, G., Kohlstedt, D., 2003. Rheology of the upper mantle and mantle wedge: a view from the experimentalists. Inside the subduction factory. *Geophysical monograph* 138, American Geophysical Union.
- Hernlund, J.W., Thomas, C., Tackley, P.J., 2005. A doubling of the post-perovskite phase boundary and structure of the Earth's lowermost mantle. *Nature* 434, 882–886.
- Jarvis, G.T., Lowman, J.P., 2007. Survival times of subducted slab remnants in numerical models of mantle flow. *Earth Planet. Sci. Lett.* 260, 23–36.
- Karato, S.-I., Zhang, S., Wenk, H.R., 1995. Superplasticity in Earth's lower mantle: evidence from seismic anisotropy and rock physics. *Science* 20, 458–461.
- Karato, S.-I., 2008. Deformation of Earth Materials. An Introduction to the Rheology of Solid Earth. Cambridge University Press (Chapter 19).
- Katsura, T. et al., 2009. P–V–T relations of MgSiO₃ perovskite determined by in situ X-ray diffraction using a large-volume high-pressure apparatus. *Geophys. Res. Lett.* 36. <http://dx.doi.org/10.1029/2008GL035658>.
- Kaufmann, G., Lambeck, K., 2000. Mantle dynamics, postglacial rebound and the radial viscosity profile. *Phys. Earth Planet. Inter.* 121, 303–327.
- King, S., Hager, B., 1994. Subducted slabs and the geoid. 1. Numerical experiments with temperature dependent viscosity. *J. Geophys. Res.* 99 (B10), 19843–19852.
- Matyska, C., Yuen, D.A., Wentzcovitch, R.M., Čížková, H., 2011. The impact of variability in the rheological activation parameters on lower-mantle viscosity stratification and its dynamics. *Phys. Earth Planet. Inter.* 188 (1–2), 1–8. <http://dx.doi.org/10.1016/j.pepi.2011.05.012>.
- Mitrovica, J.X., Forte, A.M., 2004. A new inference of mantle viscosity based upon a joint inversion of convection and glacial isostatic adjustment data. *Earth Planet. Sci. Lett.* 225, 177–189.
- Morgan, W.J., 1965. Gravity anomalies and convection currents. 1. A sphere and cylinder sinking beneath the surface of a viscous fluid. *J. Geophys. Res.* 70 (24), 6175–6187.
- Nakada, M., Karato, S.-I., 2012. Low viscosity of the bottom of the Earth's mantle inferred from the analysis of Chandler wobble and tidal deformation. *Phys. Earth Planet. Inter.* 192–193, 68–80.
- Nakagawa, T., Tackley, P.J., 2011. Effects of low-viscosity post-perovskite on thermo-chemical mantle convection in a 3-D spherical shell. *Geophys. Res. Lett.* 38, L04309. <http://dx.doi.org/10.1029/2010GL046494>.
- Panasjuk, S.V., Hager, B.H., 2000. Inversion for mantle viscosity profiles constrained by dynamic topography and the geoid, and their estimated errors. *Geophys. J. Int.* 143, 821–836.
- Pari, G., Peltier, R.W., 1995. Heat flow constraint on mantle convection. *J. Geophys. Res.* 100, 12731–12751.
- Paulson, A., Zhong, S., Wahr, J., 2007. Limitations on the inversion for mantle viscosity from postglacial rebound. *Geophys. J. Int.* 168, 1195–1209.
- Peltier, W.R., 1999. Global sea level rise and glacial isostatic adjustment. *Global Planet. Change* 20, 93–123.
- Ricard, Y., Vigny, C., 1989. Mantle dynamics with induced plate tectonics. *J. Geophys. Res.* 94, 17543–17559.
- Ricard, Y., Wuming, B., 1991. Inferring viscosity and the 3-D density structure of the mantle from geoid, topography and plate velocities. *Geophys. J. Int.* 105, 561–572.
- Spakman, W., Hall, R., 2010. Surface deformation and slab–mantle interaction during Banda arc subduction rollback. *Nat. Geosci.* 3, 562–566.
- Steinbach, V., Yuen, D.A., 1994. Effects of depth-dependent properties on the thermal anomalies produced in flush instabilities from phase transitions. *Phys. Earth Planet. Inter.* 86, 165–183.
- Steinberger, B., Calderwood, A.R., 2006. Models of large-scale viscous flow in the Earth's mantle with constraints from mineral physics and surface observations. *Geophys. J. Int.* 167, 1461–1481.
- Steinberger, B., Torsvik, T.H., 2010. Toward an explanation for the present and past locations of the poles. *Geochem. Geophys. Geosyst.* 11 (6). <http://dx.doi.org/10.1029/2009GC002889>.
- Steinberger, B., Torsvik, T.H., 2011. A geodynamic model of plumes from the margins of large low shear velocity provinces. *Geochem. Geophys. Geosyst.* <http://dx.doi.org/10.1029/2011GC003808>.
- van den Berg, A.P., van Keken, P.E., Yuen, D.A., 1993. The effects of a composite non-Newtonian and Newtonian rheology on mantle convection. *Geophys. J. Int.* 115, 62–78.
- van den Berg, A.P., Yuen, D.A., 1996. Is the lower mantle rheology Newtonian today? *Geophys. Res. Lett.* 23, 2033–2036.
- van der Meer, D.G., Spakman, W., van Hinsbergen, D.J.J., Amaru, M.L., Torsvik, T.H., 2010. Towards absolute plate motions constrained by lower-mantle slab remnants. *Nat. Geosci.* 3, 36–40.
- van der Hilst, R., 1995. Complex morphology of subducted lithosphere in the mantle beneath the Tonga trench. *Nature* 374, 154–157.
- van Hunen, J., van den Berg, A.P., Vlaar, N.J., 2000. A thermo-mechanical model of horizontal subduction below an overriding plate. *Earth Planet. Sci. Lett.* 182, 157–169.
- van Hunen, J., van den Berg, A.P., Vlaar, N.J., 2002. On the role of subducting oceanic plateaus in the development of shallow flat subduction. *Tectonophysics* 352, 317–333.
- Zhong, S., Gurnis, M., 1995. Mantle convection with plates and mobile, faulted plate margins. *Science* 267, 838–843.